nature energy

ARTICLES

https://doi.org/10.1038/s41560-019-0490-3

Facet-dependent active sites of a single Cu_2O particle photocatalyst for CO_2 reduction to methanol

Yimin A. Wu[1,2], Ian McNulty[1], Cong Liu[3], Kah Chun Lau[4,5], Qi Liu[6], Arvydas P. Paulikas[4], Cheng-Jun Sun[7], Zhonghou Cai[7], Jeffrey R. Guest[1], Yang Ren[7], Vojislav Stamenkovic[4], Larry A. Curtiss[4], Yuzi Liu[1]* and Tijana Rajh[1]*

Atomic-level understanding of the active sites and transformation mechanisms under realistic working conditions is a prerequisite for rational design of high-performance photocatalysts. Here, by using correlated scanning fluorescence X-ray microscopy and environmental transmission electron microscopy at atmospheric pressure, in operando, we directly observe that the (110) facet of a single Cu_2O photocatalyst particle is photocatalytically active for CO_2 reduction to methanol while the (100) facet is inert. The oxidation state of the active sites changes from Cu(I) towards Cu(II) due to CO_2 and H_2O co-adsorption and changes back to Cu(I) after CO_2 conversion under visible light illumination. The Cu_2O photocatalyst oxidizes water as it reduces CO_2. Concomitantly, the crystal lattice expands due to CO_2 adsorption then reverts after CO_2 conversion. The internal quantum yield for unassisted wireless photocatalytic reduction of CO_2 to methanol using Cu_2O crystals is ~72%.

Efficient catalytic reduction of CO_2 into liquid fuels can play an integral role in potentially mitigating and resolving the challenge of climate change. Previous studies have focused on CO_2 reduction by hydrogenation at elevated temperatures[1–4] although use of hydrogen raises cost and safety issues. Recently, electroreduction of CO_2 has aroused considerable interest[5–10]. However, this process requires a large overpotential[8,11] and may cause decomposition of generated chemicals[12]. Additionally, use of electricity as a secondary form of energy is inefficient due to losses associated with conversion from primary sources as well as storage and transmission.

Photoreduction of CO_2 using sunlight offers an efficient way to directly store solar energy in the form of chemical fuels. Of particular interest is its conversion directly into liquid fuels such as methanol[13]. In theory, combined photovoltaic-electrolysis approaches have lower 'solar-to-fuel' efficiency than photocatalysis due to the energy losses associated with additional conversion steps from solar to electricity and the subsequent conversion to fuels. Photocatalysis is a promising method of converting solar energy to fuel without secondary energy losses and it can potentially be scaled up for large-scale applications[14]. Unfortunately, despite intensive efforts since 1978 (ref. [15]), the photocatalysts developed for CO_2 reduction suffer from poor stability[16,17], low efficiency in the visible part of the solar spectrum[18], high cost as a result of the use of low-abundance elements[19] and low multi-electron transfer necessary for chemical fuel production[20].

Cu compounds are promising photocatalysts with good multi-electron transfer properties[21] because of their loosely bonded *d* electrons. Although in their relative infancy[22], such catalysts show great potential for facilitating CO_2 activation and conversion to CO (refs. [7,8,23,24]) or ethylene[25–27] by electroreduction, as well as for water splitting[28,29], solar cells[30] and Li ion batteries[31]. Furthermore, Cu_2O is an inexpensive material based on relatively abundant elements. Cu_2O is a direct-gap semiconductor with a band gap of 2.1 eV enabling the absorption of visible light that constitutes most of the solar spectrum[28]. Importantly, it shows intrinsic p-type conductivity due to the presence of negatively charged Cu vacancies and possesses one of the lowest electron affinities of the elements. This makes Cu_2O a good candidate for the reduction of one of the most resilient compounds, namely CO_2 (refs. [32–35]). Previous studies have focused on traditional statistical ex situ ensemble bulk measurements. Solar-to-fuel efficiencies reported for unassisted wireless photocatalytic CO_2 reduction vary across laboratories; however, in general, they are substantially smaller compared to electrical to chemical fuel efficiency in photoelectrochemical cell devices[36,37]. To design highly efficient one-step CO_2 reduction using unassisted wireless photocatalysis in neutral pH, we need to design a photocatalyst with selective active sites. However, identification of the selective active sites by traditional ex situ ensemble methods is difficult or even impossible because of the inhomogeneity of the active sites and their sensitivity to their local environment.

Here, we report the facet specific active sites in Cu_2O capable of binding and reducing CO_2. This is unravelled using operando multimodal correlated characterization of a single particle, ex situ ensemble measurements and density functional theory (DFT) calculations. Through this approach, we exploit our understanding of the facet selective active sites to design nanoparticles with improved activity. We report a photocatalytic conversion of CO_2 with liquid fuel methanol as the sole product of photoreduction where the internal quantum yield is ~72% and the solar-to-fuel efficiency is 10% with the major oxidation products being O_2 and H_2O_2.

---

[1]Center for Nanoscale Materials, Argonne National Laboratory, Argonne, IL, USA. [2]Department of Mechanical and Mechatronics Engineering and Waterloo Institute for Nanotechnology, University of Waterloo, Waterloo, Ontario, Canada. [3]Chemical Sciences and Engineering Division, Argonne National Laboratory, Argonne, IL, USA. [4]Materials Science Division, Argonne National Laboratory, Argonne, IL, USA. [5]Department of Physics and Astronomy, California State University, Northridge, CA, USA. [6]Department of Physics, City University of Hong Kong, Hong Kong, China. [7]Advanced Photon Source, Argonne National Laboratory, Argonne, IL, USA. *e-mail: yuziliu@anl.gov; rajh@anl.gov

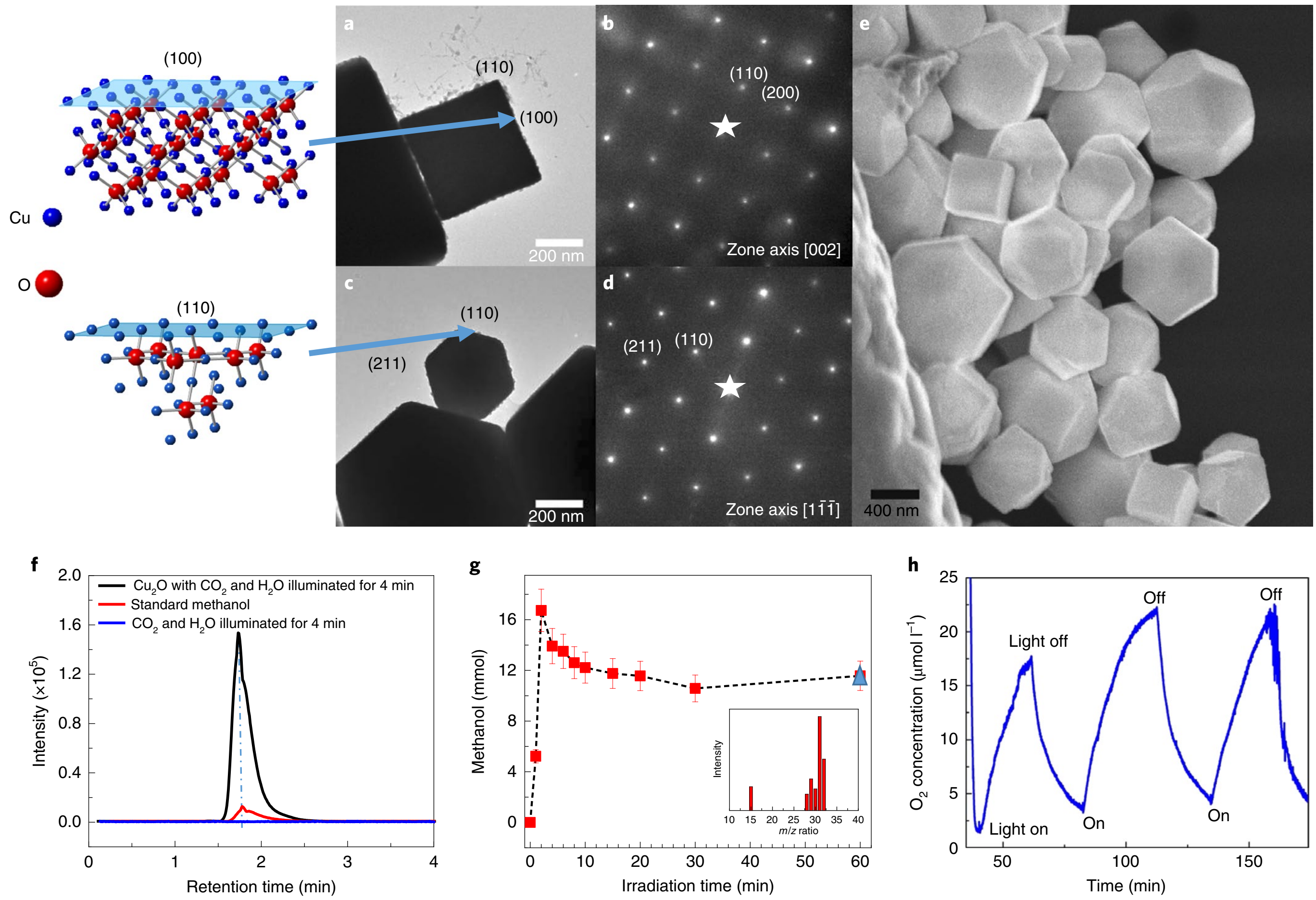

Fig. 1 | Structure, characterization and photocatalytic performance of the Cu_2O photocatalyst particles. **a**, Atomic model of Cu terminated by the (100) surface of Cu_2O used for DFT calculations and a TEM image of a single cubic Cu_2O nanocrystal with well-defined facets. **b**, NBD from the edge of the nanocrystal in **a**, indicated by the blue arrow. **c**, Atomic model of Cu terminated by the (110) surface of Cu_2O used for DFT calculations and a TEM image of another particle with a hexagonal projected shape and well-defined facets. **d**, NBD on the edge of **c**, indicated by the blue arrow. **e**, SEM image of the cubic/octahedral sample. **f**, Methanol production by the cubic/octahedral sample measured by GC during the photocatalytic reaction as a function of retention time (black lines), the standard methanol measured by GC (red lines) and the control experiment with CO_2 and H_2O but without Cu_2O by GC (blue lines). The dot-dashed line indicates the same retention times of the black-line and red-line peaks. a.u., arbitary units. **g**, Illumination time-dependent conversion of methanol produced by the photocatalytic reaction using CO_2 and liquid H_2O (red squares) and using CO_2 and H_2O vapour (blue triangles). The error bars are 10% of the average value of five measurements. Inset: mass spectra of methanol obtained by GC–MS analysis of the photocatalytic reaction products. **h**, O_2 evolution during CO_2 reduction photocatalysis.

Characterization of photocatalytic materials

We prepared Cu_2O nanocrystal samples with well-defined (110) and (100) facets via colloidal synthesis (see Methods and Supplementary Fig. 1). Two types of Cu_2O samples were synthesized (Fig. 1 and Supplementary Fig. 2): one containing a mixture of cubic and octahedral nanocrystals and the other primarily composed of cubic nanocrystals. Characterization of the first sample, which consisted of cubic/octahedral particles, by transmission electron microscopy (TEM) showed various projections of Cu_2O crystals with well-defined facets and noticeable truncations at the corners (Fig. 1). Nanobeam electron diffraction (NBD) showed (110) and (200) facets with a [002] zone axis (Fig. 1b). This indicates that the particle shown in Fig. 1a is a cube enclosed by (100) facets with (110) facets at the truncated corners. Particles with a hexagonal projected shape were also observed (Fig. 1c) with a [1$\bar{1}\bar{1}$] zone axis, (110) edges and (211) corners seen by NBD (Fig. 1d). All Cu_2O crystals were cubic phase with space group *Pn*$\bar{3}$*m*, which were confirmed both by TEM and X-ray powder diffraction measurements. Scanning electron microscopy (SEM) showed that the truncated cubic/octahedral crystals were 500 nm to 1 μm in size (Fig. 1e).

The illumination of faceted Cu_2O nanoparticles in the presence of CO_2 and water showed the formation of a new molecular product. The products of this photocatalytic reaction (Fig. 1f, black line, see Methods) showed the same retention time as the methanol analytical standard (Fig. 1f, red line) by gas chromatography (GC) analysis, while no products (Fig. 1f, blue line) were observed in the absence of the purified Cu_2O photocatalyst. The only product was methanol, as confirmed by gas chromatography mass spectrometry (GC–MS) that showed peaks with mass-to-charge ratios of 32, 31, 30, 29, 28 and 15 (Fig. 1g, inset), corresponding to $[CH_3OH^\bullet]^+$, $[CH_3O]^+$, $[CH_2O]^+$, $[CHO]^+$, $[CO]^+$ and $[CH_3]^+$. The same species were obtained in a standard methanol mass spectrum (Supplementary Fig. 3).

The amount of methanol produced was determined by comparing the integrated area of the GC peaks with that of known amounts of standard pure methanol. The methanol production and its dependence on irradiation time (Fig. 1g) showed an internal quantum yield of 72% (see Methods and Supplementary Fig. 4), which is comparable to the recent reported efficiencies of 50% and 63% obtained using electroreduction[10,38]. The solar-to-fuel efficiency was measured to be 10% (see Methods), which was smaller than the theoretically predicted maximum of 35.2% (ref. [39]). The plateau in the time conversion curve (Fig. 1g) indicated that the methanol produced by photoexcited electrons reached a steady state with the same formation and consumption rate beyond 6 min of irradiation time.

Concomitantly, the system produced oxygen in synchrony with periodic illumination (Fig. 1h and see Methods), suggesting that our photocatalysts can couple H_2O oxidation with CO_2 reduction, functioning as an artificial leaf[9], albeit in a substoichiometric ratio (see Methods and Supplementary Fig. 5). Substoichiometric oxygen production was previously observed; its formation rate is typically several orders of magnitude smaller than those of the main catalytic products[40]. Some of the photogenerated holes may be consumed in the photo-induced disproportionation of Cu_2O nanoparticles, the formation of H_2O_2 (see Methods) and other reactive oxygen species (ROS) and/or in re-oxidation of methanol, contributing to the steady state in the methanol evolution. The oxygen isotope tracer experiment using oxygen-labelled water ($H_2{}^{18}O$; for details, see Methods and Supplementary Fig. 6) showed that the majority of photogenerated molecular oxygen is isotopically mixed $^{16}O^{18}O$ with small amounts of $^{18}O_2$ and $^{16}O_2$. This indicates that H_2O is the major source for the oxygen evolution reaction (although the initial water is pure $H_2{}^{18}O$, one molecule of water $H_2{}^{16}O$ is produced from each $C^{16}O_2$ converted into methanol to contribute to ^{16}O content), with a possible smaller contribution from $Cu_2{}^{16}O$ isotopic exchange. Lattice oxygen in the highly active oxide was shown to contribute to the generation of oxygen due to the hybridization of the oxygen orbital with the Fermi level of the photocatalysts[41,42]. The total amount of oxygen produced in the reaction after 2 min of illumination was 1.45 mmol (~6% efficiency). The formation of H_2O_2 was also determined to be 5.8 mmol using potassium permanganate titration (~12% efficiency). Singlet oxygen, adsorbed oxo- and peroxo- species may also be produced but their amount was hard to quantify.

Noticeably, the same amount of methanol was produced if H_2O vapour was used instead of liquid H_2O (Fig. 1g and Supplementary Fig. 7), which indicates that H_2O vapour oxidation follows a similar reaction mechanism to that of liquid H_2O. The $^{13}CO_2$ isotope tracer experiment (see Methods and Supplementary Fig. 8) showed the formation of $^{13}CH_3OH$ as the only product, with GC–MS analysis showing distinct mass-to-charge ratios of 16 and 33 corresponding to $[^{13}CH_3]^+$ and $[^{13}CH_3OH\bullet]^+$ when compared with the product from the unlabelled $^{12}CO_2$ reaction. The remaining peaks at 45 and 44 correspond to the unreacted $^{13}CO_2$ and $^{12}CO_2$ in the sealed vial, respectively (Supplementary Fig. 8). This gives strong evidence that the carbon in methanol originates from CO_2. We did not observe methanol oxidation and formation of H_2 as a by-product from H_2O reduction. This is probably due to the fast desorption of methanol from the surface of the catalyst. Methanol oxidation is relatively easy to observe using electron paramagnetic resonance (EPR) due to the doublet lines at the 130 G separation of the methanol radical and the formyl radicals[43]. However, we did not observe any similar radical during illumination of Cu_2O particles with CO_2 and H_2O in the EPR cavity at 4 K, as shown in the section 'Ensemble characterization at a statistic level'. Nevertheless, illumination of the same amount of cubic Cu_2O sample (Supplementary Fig. 2b) in the presence of CO_2 and H_2O produced only a fraction (~10%) (Supplementary Fig. 2c,d) of the methanol observed with the cubic/octahedral sample (Supplementary Fig. 2a), suggesting that the (100) facets were nearly inactive whereas the sample with higher-index facets was more active photocatalytically.

Operando multimodal characterization of single particles

To understand the role of the active sites and local crystal structure on the photoreduction of CO_2 under real working conditions, we studied single Cu_2O particles by both environmental transmission electron microscopy (ETEM) and scanning fluorescence X-ray microscopy (SFXM) in a nanoreactor[44,45] while exposed to a mixture of gaseous CO_2, H_2O and light (see Methods, Fig. 2a and Supplementary Fig. 9). For example, we first identified particle I (Fig. 2d), with a truncated hexagonal shape (red circle in Fig. 2c), by TEM. A corresponding single-particle electron diffraction (SPED) measurement indicated that the edges of particle I were {220} planes in the TEM view (Supplementary Fig. 10). Then, we transferred the nanoreactor containing the Cu_2O particles from the ETEM to the SFXM platform.

Low-resolution scans (Fig. 2e) using the Cu and Ni Kα fluorescence signals from the Cu_2O particles and grid bars, respectively, enabled us to locate the same particle I (white circle in Fig. 2e) for imaging and nanospectroscopic study by SFXM. In the high-resolution Cu Kα fluorescence image in Fig. 2f we observe particle I as a truncated square rather than a truncated hexagon observed in TEM. This was due to the relative projected views of the particle using the ETEM and SFXM platforms, which differed by nearly 60°, and can be understood by considering particle I to be a cube resting on one of its truncated corners, a (111) facet (Fig. 2b). With the TEM view directions as indicated by the red arrow, the particle appeared as a corner-truncated hexagon (Fig. 2b,d), while it presented as a corner-truncated square when viewed with X-ray imaging (Fig. 2b,f). Hence, the corner of particle I was a (110) facet while edges are exposed as a (100) facet along the X-ray view direction (Fig. 2b,f). We targeted specific facets of particle I by directing the nanofocused X-ray beam parallel to desired facets whilst scanning the incident X-ray energy (Supplementary Fig. 9), enabling us to obtain facet-dependent spectroscopic information of the Cu active sites. The spectroscopic signal, which resulted from a columnar projection of the X-ray beam through the plane of the facet, probably reflected an admixture of states resulting from both the surface and interior chemistry.

X-ray fluorescence spectra (Fig. 3a) taken near the Cu K edge on the (110) facet of Cu_2O particle I in its initial pristine state revealed a white-line peak at 8,981.0 eV, indicating a Cu(ɪ) oxidation state associated with this facet, in agreement with reference X-ray absorption spectra taken from pure Cu_2O (Supplementary Fig. 11). By contrast, the white-line peak observed on the (100) facet was at 8,981.5 eV, indicating the presence of both Cu(ɪ) and Cu(ɪɪ) oxidation states (Fig. 3a). When measuring spectra on the (110) facet before and after flushing CO_2/H_2O through the nanoreactor for a few minutes, the peak shifted of between 1.0 and 1.5 eV towards higher energy (Fig. 3b and Supplementary Fig. 12), indicating that the oxidation state of the Cu changed from oxidation state 1^+ towards 2^+ due to the co-adsorption of CO_2/H_2O. In addition, consecutive spectra measured at intervals of 10 min at another position on the (110) facet of particle I showed a gradual shift of the peak by ~1 eV until saturation was reached in about 1 h (Supplementary Fig. 12). These results suggest that CO_2/H_2O co-adsorbed on the (110) facet reduced the electron density of the exposed Cu atoms, causing the oxidation state to shift from Cu(ɪ) towards Cu(ɪɪ). Furthermore, when the particle was excited with a green laser (532 nm) while maintaining a constant CO_2/H_2O gas flow, the peak reverted back by ~1 eV towards lower energy (Fig. 3b), indicating that the majority of the Cu oxidation states shifted back to Cu(ɪ). In comparison, the oxidation states of the Cu atoms on the (100) facet did not change on CO_2/H_2O adsorption in either the dark or the illuminated states (Fig. 3c), indicating the (100) facet was photocatalytically inactive. In successive measurements on several other, similar Cu_2O particles, we reproducibly observed similar spectroscopic shifts on the (110) facets followed by reversion on illumination, and statistically insignificant shifts on the (100) facets. We note that the X-ray measurements could not have triggered the photocatalytic reaction because the chemical state

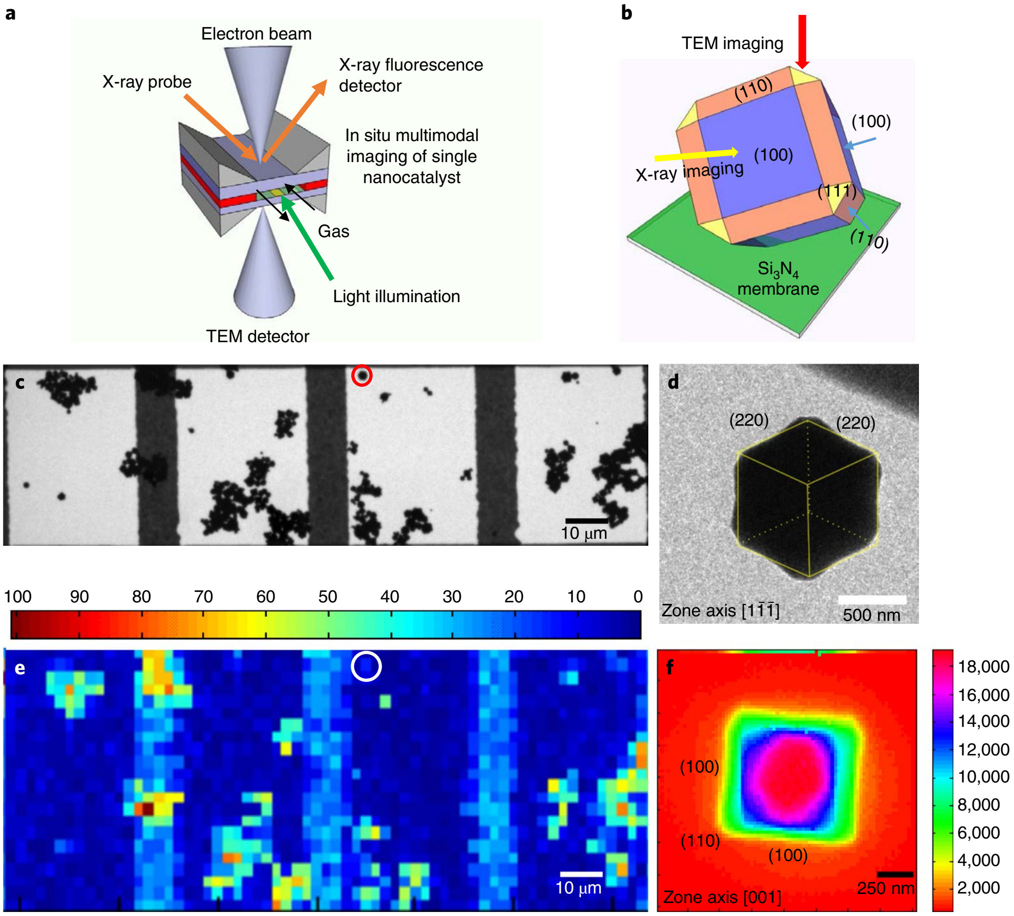

Fig. 2 | Operando multimodal imaging of a single photocatalyst Cu_2O particle. a, Schematic illustration of the setup showing the gas-flow nanoreactor. **b**, Schematic of the electron beam and X-ray directions for TEM and SFXM imaging on particle I, a truncated cube. **c**, TEM overview of Cu_2O particles inside the nanoreactor. The red circle indicates particle I. **d**, TEM image showing particle I with the electron beam parallel to the [1$\bar{1}\bar{1}$] direction of the Cu_2O cube. **e**, Low-resolution SFXM image of the particles inside the nanoreactor from Cu Kα and Ni Kα emission with a white circle indicating particle I. The different aspect ratios between **c** and **e** are due to the 60° difference between the X-ray and TEM imaging directions. **f**, High-resolution SFXM image of particle I from Cu Kα emission with the incident X-ray beam parallel to the [001] direction. The colour scales in **e** and **f** indicate the intensity of the Cu fluorescence signal. The units in the colour bars are arbitrary.

of the Cu in the pristine Cu_2O did not change over the course of many measurements without the introduction of gas, and it did not change from Cu(II) to Cu(I) until subsequent optical illumination (Supplementary Fig. 12).

Particle I was checked again by TEM and SPED after the X-ray measurements, which showed that the location and structure of particle I were preserved (Supplementary Fig. 13). This finding rules out the possibility that the particle moved or was significantly damaged structurally by the X-ray beam. While we characterized the same Cu_2O particles by both ETEM and SFXM, it should be noted that in TEM the particle could not be tilted to the same view orientation as for the SFXM measurements. To verify these results we used ETEM to examine another Cu_2O particle in the nanoreactor, the truncated cube particle II, with the same orientation as particle I that we studied with X-ray imaging (we could not tilt particle I due to geometric limitations). SPED measurements confirmed the presence of {110} facets on the truncated corners and {100} facets on the faces of particle II (Supplementary Fig. 10), as with particle I in the X-ray measurements. Electron energy loss spectra (EELS) recorded on the (110) facet before and after CO_2/H_2O co-adsorption in the dark state showed that the Cu $L_{2,3}$ edge (2*p* to 3*d* transition) shifted ~2 eV towards lower energy on CO_2/H_2O adsorption (Fig. 3d). The EELS spectrum from the pristine particle (Fig. 3d, black line) is consistent with the peak position and L_3/L_2 peak intensity ratio of Cu_2O (ref. [46]). The broadening of the spectrum recorded with gas flow (Fig. 3d, red line) and the decrease in the L_3/L_2 peak intensity ratio indicate the formation of Cu^0. The energy shift between the spectral peaks of the particles taken before and after gas adsorption (Fig. 3d, black and red lines) shows that, of the superposition of copper phases present, Cu(II) dominates because the L_3 peak energies of Cu^0 and Cu(I) are the same. This is further quantified by EPR with much higher sensitivity described in section 'Ensemble characterisation at a statistic level'. Similar energy shifts were observed by EELS on the particle III and particle IV (110) facets (Supplementary Fig. 12). These shifts are consistent with the oxidation state change from Cu(I) to Cu(II) seen with X-ray imaging[46]. Again, consistent with the X-ray measurements, the EELS data did not show a change in the Cu oxidation state on the (100) facet.

We also carried out DFT calculations to understand the mechanism of CO_2 and H_2O adsorption on Cu_2O on different facets (Fig. 4a,b). The calculations showed that the co-adsorption of CO_2 and H_2O are thermodynamically favourable on both the (110) and (100) facets (Cu termination was considered for both facets), although the co-adsorption on (110) is much more favourable (energy of adsorption, $E_{ad} \approx -2.8$ eV) than that on (100) ($E_{ad} \approx -1.87$ eV). It is notable that the co-adsorption of CO_2 and H_2O

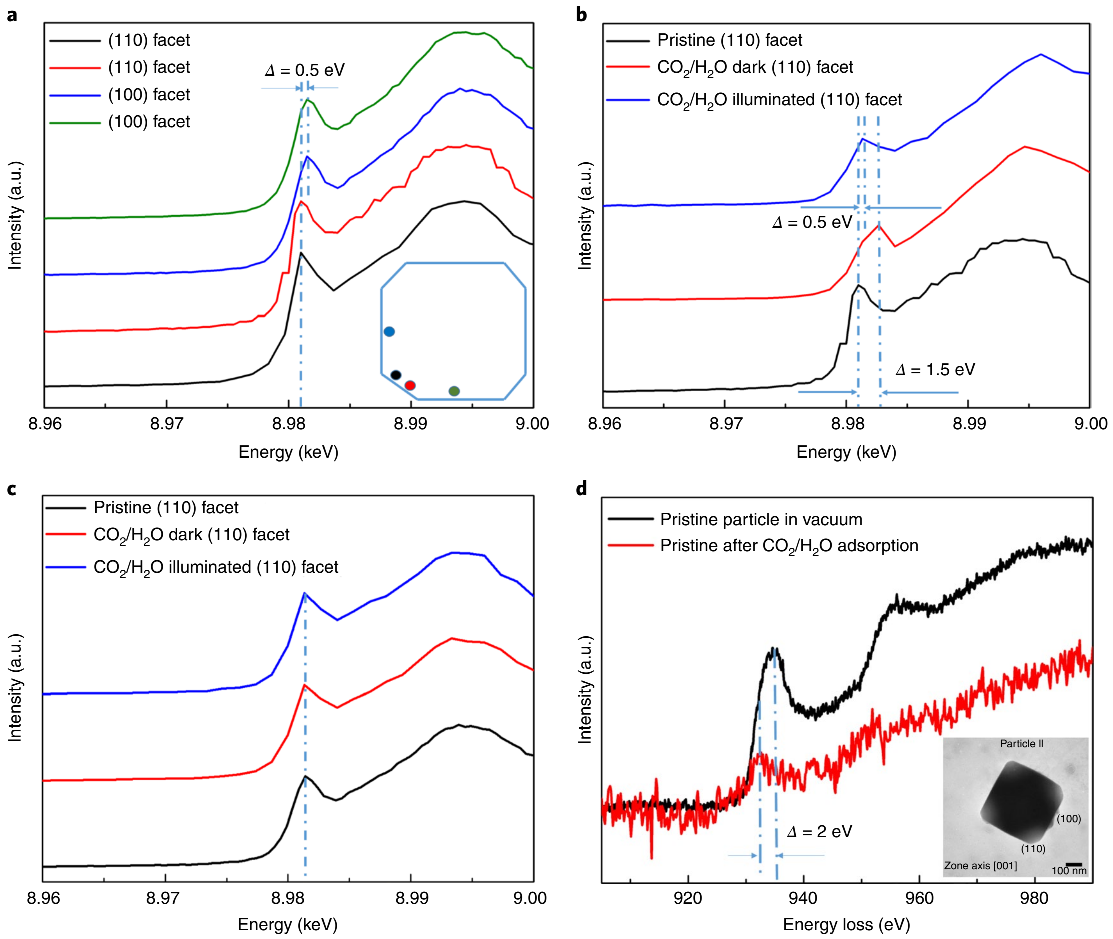

Fig. 3 | Operando multimodal nanospectroscopy of a single photocatalyst Cu_2O particle under various working conditions. a, Scanning X-ray nanospectroscopy of various facets of particle I (Fig. 2f) in the pristine state. Δ denotes the shift in the white line peak in the Cu K-edge X-ray spectrum. Inset: the locations for spectra recorded from particle I, with the corresponding colours indicated. **b**, Oxidation state changes at the (110) facet of particle I in the pristine state, with CO_2/H_2O gas exposure under dark and under illuminated conditions. **c**, Oxidation states at the (100) facet of particle I under the same conditions. **d**, In situ EELS on the (110) facet of particle II. Inset: the TEM images of particle II. The lower signal-to-noise ratio of the spectrum taken with gas is due to greater electron scattering in comparison to in vacuum. a.u., arbitrary units.

on Cu-terminated (110) led to a dramatic change of the arrangement of Cu atoms on the surface leading to the formation of Cu clusters (Fig. 4a,c,d). This was confirmed by the EPR measurements. This cluster formation, however, did not occur on either the Cu/O-terminated (the termination have both Cu and O atoms) (110) or the Cu-terminated (100) on CO_2 and H_2O adsorption, based on our calculations (Fig. 4b,e,f). This suggests that the (110) facets of the synthesized Cu_2O particles are likely to be Cu terminated and therefore have greater photocatalytic activity for co-adsorption of CO_2 and H_2O. This also indicates that the surface termination of Cu_2O has a strong effect on the photocatalytic reaction activity and may affect the final product from the reaction. We carried out further calculations and found that, among all the Cu_2O surfaces we considered, only CO_2 co-adsorption with H_2O on the Cu-terminated Cu_2O (110) leads to bent CO_2 (CO_2^-) (Supplementary Fig. 14), and the conversion from a physisorbed CO_2 to a bent CO_2 on this surface is energetically favourable ($\Delta E = -6.3$ eV). Such a highly exergonic reaction indicates that the first energy barrier for the reduction could be low. For the Cu/O-terminated Cu_2O (110) and all the Cu_2O (100) terminations, the geometry optimizations show that the bent CO_2 is not stable on these surfaces. Our calculations also show that, without H_2O co-adsorption, the bent CO_2 is not stable on any of the considered surfaces.

Ensemble characterization at a statistical level

We characterized the properties of the ensembles of Cu_2O particles by high-resolution X-ray powder diffraction (HRXRD) and EPR to obtain complementary information about the photocatalytically active sites. Operando high-energy X-ray diffraction measurements (Supplementary Fig. 15) show the absence of noticeable structural changes (no line broadening, disappearance/appearance of additional lines or decrease of line intensity) in the Cu_2O particles over 8 h during the photocatalytic reaction. The stability is also confirmed by the ex situ X-ray photoemission spectroscopy. Formation of strong Cu 2*p* satellite peaks, characteristic of oxidized CuO samples, were not observed in both pristine and reacted Cu_2O catalyst (Supplementary Fig. 16). Fine structural changes in the Cu_2O particles were probed ex situ using HRXRD (Fig. 5a). In the HRXRD data in Fig. 5b,c, we see that CO_2/H_2O co-adsorption under dark conditions increased the crystal lattice constant, which is consistent with our spectroscopic observation (Fig. 3b) that the CO_2 withdrew the electron density from the Cu active sites, leading to an oxidation state change from Cu(I) to Cu(II). Consistently, using DFT calculations we found substantial charge transfer at the co-adsorption sites of CO_2 and H_2O at the Cu-binding site of the (110) surface (Fig. 5f). Relative to bulk crystalline Cu_2O with Cu–O bond lengths of 1.86 Å, the Cu–O bonds in the vicinity of the CO_2 and H_2O co-adsorption

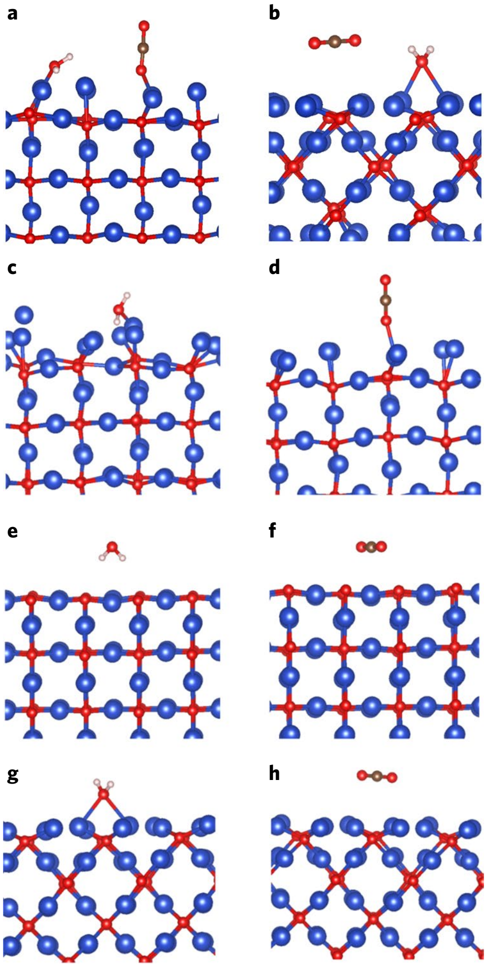

Fig. 4 | DFT calculations of binding energies. **a**, Confirmation of CO_2/H_2O co-adsorption on Cu_2O (110) Cu termination. The binding energy is −2.8 eV. **b**, Confirmation of CO_2/H_2O co-adsorption on Cu_2O (100) Cu termination. The binding energy is −1.87 eV. **c**, Individual binding confirmation of H_2O on Cu_2O (110) Cu termination. The binding energy is −1.04 eV. **d**, Individual binding confirmation of CO_2 on Cu_2O (110) Cu termination. The binding energy is −5.27 eV. **e**, Individual binding confirmation of H_2O on Cu_2O (110) Cu/O termination. The binding energy is −0.21 eV. **f**, Individual binding confirmation of CO_2 on Cu_2O (110) Cu/O termination. The binding energy is −0.10 eV. **g**, Individual binding confirmation of H_2O on Cu_2O (100) Cu termination. The binding energy is −0.75 eV. **h**, Individual binding confirmation of CO_2 on Cu_2O (100) Cu termination. The binding energy is −0.79 eV. The Cu, O, C and H atoms are shown in blue, red, brown and white, respectively.

sites were found to be about 1.92–1.95 Å by DFT calculations, which is very similar to the DFT computation of 1.95 Å in bulk crystalline CuO. After optical illumination (Fig. 5b,c, blue lines), the lattice constant of pristine Cu_2O was recovered (Fig. 5b,c, black lines).

The above results suggest that, on co-adsorption of CO_2/H_2O on Cu_2O particles, intermolecular electron transfer occurs between the Cu active sites at the (110) surfaces and CO_2 molecules. This redistribution of electron density results in partial reduction of adsorbed CO_2/H_2O molecules, lowering the energy barrier for their complete reduction. On the other hand, the electron redistribution reduces the electron density of the (110) surface. This in turn facilitates localization of photogenerated electrons on these sites, enhancing the probability of their interaction with adsorbed molecules. Illumination of CO_2/H_2O co-adsorbed on the (110) facet, therefore, leads to efficient electron transfer and removal of the bonding between CO_2 molecules and active sites, restoring the electron density of the pristine Cu_2O. Co-adsorption of CO_2/H_2O by the particles is consistent with the lattice constant changes seen by HRXRD (Fig. 5b,c and Supplementary Fig. 17), which suggest volumetric expansion and possible CO_2 induced lattice strain. Similar behaviour has been observed in Au nanoparticles undergoing CO or thiol gas adsorption[47,48].

The complementary role of the adsorbed water to that of CO_2 reduction gives strong corroboration of the photocatalysis process. Besides providing protons for the photocatalytic reaction, HRXRD studies of water adsorption on Cu_2O particles indicate that the H_2O molecule donates electrons and pushes the electron density towards the Cu_2O surface (Supplementary Fig. 18). However, the reverse Cu oxidation state change on co-adsorption of CO_2 and H_2O (Fig. 3b) indicates the dominating effect of CO_2 over H_2O.

To investigate binding and electron transfer between Cu active sites and CO_2 molecules, we made EPR measurements on pristine Cu_2O particles, exposed to CO_2/H_2O under dark and illuminated conditions (Fig. 5d). The pristine particles (Fig. 5d, black lines) showed the existence of Cu(II) defects with unpaired electrons in 3*d* orbitals consistent with the *p*-doping of Cu_2O nanoparticles with g tensor characteristic of magnetic moment and anisotropy of copper ions. The spectral shape suggests that the loosely packed pristine Cu_2O powder is aligned in the magnetic field[49]. The hyperfine pattern of typical Cu complexes disappears in favour of a new aligned single-crystal signal at intermediate *g* with large and almost unresolved hyperfine splitting[50]. On CO_2 adsorption in the dark, however, the anisotropy of the Cu_2O powder spectrum and a hyperfine splitting (*A*) pattern reappears (Fig. 5d, red lines). The full anisotropic spectrum of saturated coordinated Cu(II) is, however, restored only by CO_2/H_2O co-adsorption (Fig. 5d, blue lines). In this case, the restored *g* and *A* tensors ($A_{\parallel}$ for Cu of 137 G and $g_{\parallel}$ of 2.3420) provide evidence for a distorted tetrahedral complex rather than octahedral or square planar coordination, which is typically found for Cu complexes[51]. This indicates the proximity effect of H_2O and CO_2 co-adsorbed on the same Cu(II) defect and the structural changes of surface defects (Cu(II), unpaired spin) under adsorption. The overall intensity of the spectrum was increased, suggesting the number of spins, and consequently the number of Cu(II) ions, increased on CO_2 and H_2O co-adsorption in the dark. This suggests that the CO_2 molecules are withdrawing electron density from Cu(I) active sites, in agreement with our X-ray spectroscopic and structural observations (Figs. 3b and 5a–c). The CO_2 and H_2O co-adsorption increases spin density (Cu(II)) isotopically (Fig. 5d, blue lines), compared to CO_2 adsorption alone (Fig. 5d, red lines) in the dark. This indicates H_2O co-adsorption can facilitate CO_2 adsorption.

A new weak peak with $g = 2.0023$ was observed with illumination of Cu_2O at 4 K (Fig. 5e and Supplementary Fig. 19). This signal originates from the conduction electrons in the metallic Cu clusters formed on illumination[52]. Formation of Cu clusters may play an important role in electron–hole pair separation and catalytic conversion of CO_2 and H_2O to methanol by lowering the energy barrier and providing a reaction pathway for methanol formation[1,53] as single-atom catalysts. Small Cu^0 clusters can also have strong adsorption strength to the adsorbate species due to the undercoordinated bonds. The Cu clusters can also act as plasmonic centres to enhance the electrical field around the adsorbates while having minor thermal effects on the particle and its surroundings, due to weak electron photon coupling and smaller absorption cross-section compared to nanoparticles. The synergetic interplay between Cu(I) and Cu clusters may be the reason for this high selectivity and high efficiency of methanol formation.

The formation of Cu clusters may be a consequence of the Cu_2O disproportionation reaction. While the X-ray nanospectroscopy and

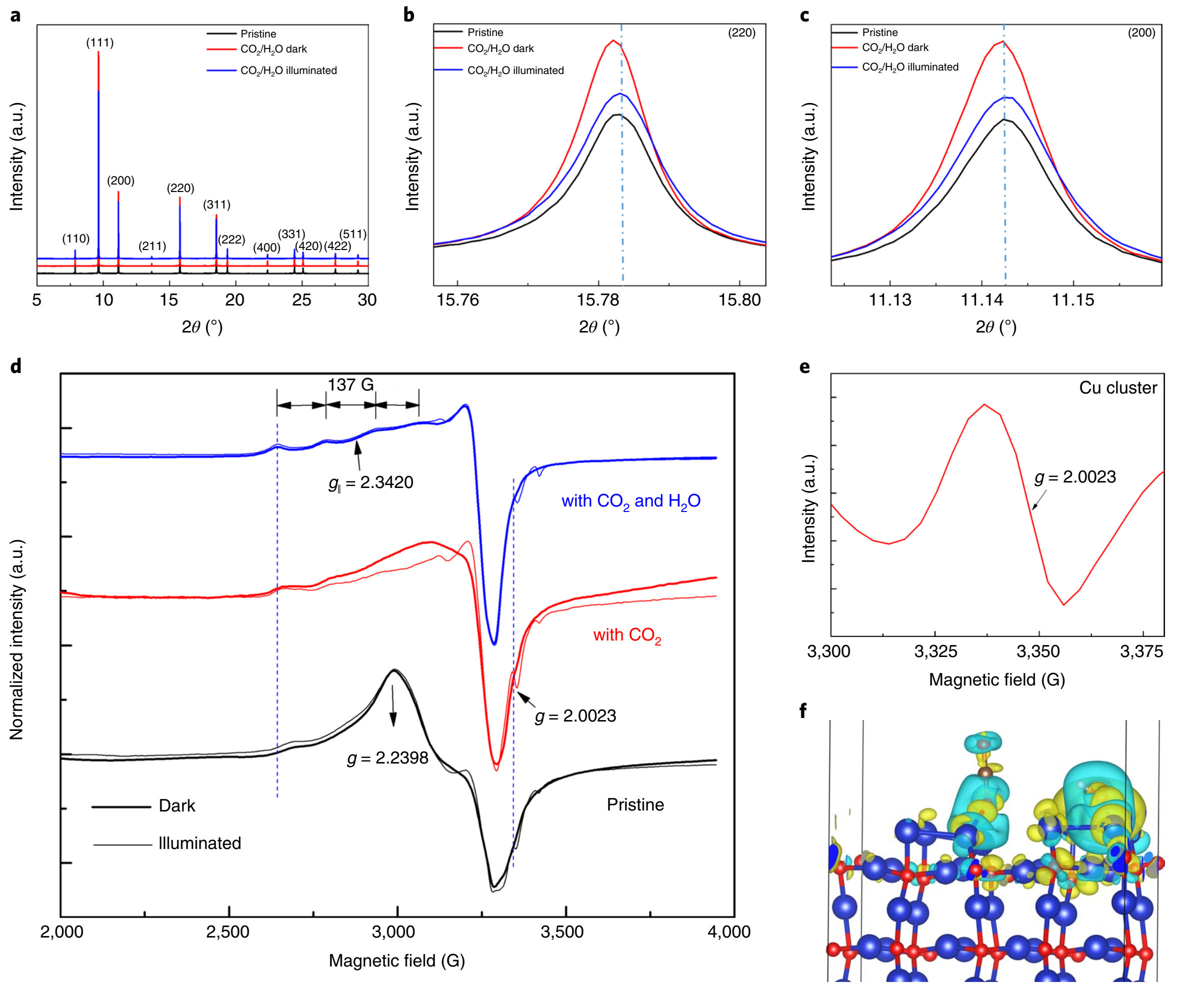

Fig. 5 | Ex situ ensemble-averaged measurement of Cu_2O particles and charge transfer. **a**, HRXRD measurements, showing that Cu_2O crystals were cubic phase with space group $Pn\bar{3}m$. **b**, Close-up view of the (220) peak, showing a noticeable shift. **c**, Close-up view of the (200) peak. **d**, Dark EPR spectra (thicker solid lines) of Cu_2O particles, showing adsorption induced electron transfer between Cu_2O particles, CO_2 and H_2O. Light-induced EPR spectra (thinner solid lines), show redistribution of the electron transfer between the Cu_2O particles, CO_2 and H_2O with simulated sunlight illumination. The g-factor represents the characteristic magnetic moment and anisotropy of the investigated paramagnetic species. **e**, Formation of Cu clusters under illumination. $g = 2.0023$ is a g-factor of free electrons and is characteristic for collective plasmon orbitals of small clusters. **f**, DFT calculation showing that a substantial charge transfer takes place between the adsorbed CO_2 and H_2O on Cu-binding sites at the (110) facet that leads to the change of Cu–O bonds on the surfaces, as discussed in the text. The black lines represent the periodic boundaries of the simulation cell, the yellow and light blue shaded regions represent the electronic charge transfer of the system. The Cu, O, C and H atoms are shown in blue, red, brown and white, respectively.

EELS measurements probed the dominant formation of Cu(ɪɪ), they were not sensitive enough to probe the formation of a small quantity of Cu clusters. Herein, the disproportionation reaction was quantified by EPR and found to be seven orders less than the yield of the main photocatalytic reaction and O_2 generation (4.98×10^{-12} mol, see Methods). Hence, the observed O_2 evolution (Fig. 1h) does not only originate from Cu(ɪ) disproportionation. Consistent with oxidation state (Fig. 3b) and structural measurements (Fig. 5b), the number of Cu(ɪɪ) ions decreased after illumination, suggesting the conversion of Cu(ɪɪ) into non-paramagnetic Cu(ɪ).

All the above evidence indicates that the adsorption effect is the dominant effect on CO_2 photocatalytic reduction on Cu_2O facets. The photoreduction of other electron accpetors such as Au ions does not show obvious charge separation efficiency differences between the (110) and (100) facets (see Methods and Supplementary Fig. 20), in contrast to previously reported spatial charge separation efficiency heterogeneity for water splitting[54]. These results suggest that the coating of Cu_2O particles with other materials, such as graphene oxide[34], could change the adsorption sites and active sites and lead to different reaction pathways that would produce different products instead of methanol.

Conclusions

Our material design strategy, which integrated X-ray and electron microscopy, bulk X-ray diffraction and EPR methods with DFT calculations, enabled us to correlate the electronic structure with the atomic structure, both at the single-particle and ensemble levels. It was found that the electron density of the Cu active sites on the (110) facet shifted from Cu(ɪ) to Cu(ɪɪ) on co-adsorption of CO_2/H_2O. Under 532 nm illumination, the Cu oxidation state changed from Cu(ɪɪ) back to Cu(ɪ), which indicates bond breakage between the CO_2 and Cu active sites. These changes were accompanied by a volumetric response to photocatalytic stimulation. CO_2 was reduced by accepting photogenerated electrons while the H_2O was oxidized by accepting photogenerated holes. The disproportionation reaction of Cu_2O might be a part of the photocatalytic process but the yield was seven orders of magnitude lower than the major photocatalytic reaction. The oxidation state of the (100) facet remained unchanged on CO_2 adsorption under both dark and illuminated conditions, indicating that the (100) facet is photocatalytically inert.

We anticipate that this facet-dependent single-particle approach can be extended to design other catalytic materials displaying site-specific behaviour, such as two-dimensional (2D) nanoplatelets and thin films of Cu_2O with large-area (110) surfaces. We further expect that Cu_2O, with its site-specific photocatalytic reduction of CO_2, small electron affinity and large reduction potential, and a band structure optimized for charge pair formation and adsorption of solar radiation, will inspire the development of new classes of materials offering a path towards CO_2 utilization as well as efficient conversion of solar energy into chemical liquid fuels.

Methods

Synthesis of Cu_2O photocatalyst particles. We synthesized two types of Cu_2O samples, one containing a mix of cubic and octahedral nanocrystals (Supplementary Fig. 2a) and the other primarily composed of cubic nanocrystals (Supplementary Fig. 2b) using standard colloidal synthesis methods[55].

To synthesize the cubic/octahedral Cu_2O sample, deionized water (88.2 ml), $Cu(CH_3COO)_2$ aqueous solution (5 ml, 0.1 M) and sodium dodecyl sulfate (0.87 g) were successively added into a three-neck flask. The three-neck flask was placed in a water bath at 60 °C with vigorous magnetic stirring. After complete dissolution of the sodium dodecyl sulfate powder in 1 h, NaOH solution (1.8 ml, 1.0 M) and D-(+)-glucose aqueous solution (5 ml, 0.1 M) were successively quickly injected into the flask. The total volume of the solution was 100 ml. The flask was kept in a water bath at 60 °C after the injection under vigorous magnetic stirring for 1 h. The solution colour gradually changed from blue to green, yellow, orange and finally brick-red (Supplementary Fig. 1). After the reaction, the precipitate was separated from the solution by centrifugation at 5,000 r.p.m. for 5 min and washed several times with deionized-water–ethanol solution.

Synthesis of the cubic Cu_2O sample was performed by dissolving $CuCl_2{\bullet}2H_2O$ (0.171 g) into aqueous solution (100 ml). NaOH aqueous solution (10 ml, 2.0 M) was then added drop-wise into the above transparent light green solution. After vigorous magnetic stirring for 0.5 h, ascorbic acid solution (10 ml, 0.6 M) was added to the solution. The colour of the liquid changed gradually from black to turbid red. The mixture was aged for 3 h. All procedures were carried out under constant vigorous magnetic stirring and heated at 55 °C. The resulting precipitate was separated from the solution by centrifugation at 5,000 r.p.m. for 5 min and washed several times with deionized water and ethanol.

All the particles were washed and purified to remove ligands after the synthesis. Both samples were dried inside a N_2 gas-flow glove box under room temperature for 48 h and then stored inside the N_2 gas-flow glove box to avoid any contamination from organics for later characterization. All chemicals were purchased from Sigma Aldrich.

Photocatalytic activity characterization. We characterized the photocatalytic activity of both Cu_2O particle syntheses by measuring their methanol production (Supplementary Fig 4c,d). In a typical reaction, 0.01 g of purified particles were dispersed in 5 ml of ultrapure deionized H_2O in a 20-ml Agilent Headspace vial and sealed. The suspension was thoroughly degassed to remove air with CO_2 gas for 10 min. CO_2 gas (Airgas, Inc.) was bubbled through a deionized H_2O bubbler glassware for the CO_2/H_2O gas mixture. The suspension was continuously flushed with the CO_2/H_2O gas mixture for another 30 min to saturate the suspension with CO_2. Then the suspension was illuminated using a 300 W Xe lamp (Perkin-Elmer Optoelectronics) at a power of 204 W with continuous CO_2/H_2O gas flow for 0–60 min. The sealed suspension was removed from the gas line after illumination. The methanol in both the gaseous product and the liquid in aqueous solution was extracted out at a temperature above the boiling point of methanol and then injected for quantification using an Agilent Headspace sampler (model 7697 A) connected to an Agilent GC–MS analyser (model 5975C GC–MS, with quadrupole detector, thermal conductivity detector (TCD) detector, DB-5ms column and helium carrier gas). Standard methanol (LC–MS ultra CHROMASOLV, tested for UHPLC–MS) was purchased from Fluka. The formation rate of methanol is about 1.2 $mol\,g^{-1}h^{-1}$. For quantification of oxygen, CO_2 was saturated in suspension first. Then the suspension was illuminated using a 300 W Xe lamp (Perkin-Elmer Optoelectronics) at a power of 204 W for 2 min in the sealed headspacer without any gas flow. The amount of oxygen in gas phases was extracted for the quantification in GC (Supplementary Fig. 5). The dissolved oxygen in H_2O was calculated using the solubility of 8.6 $mg\,l^{-1}$.

In situ oxygen measurement was performed using an oxygen needle sensor from Unisense. A mass of 0.01 g of purified particles was dispersed in 20 ml of ultrapure deionized H_2O in an Agilent Headspace vial and sealed. The oxygen needle sensor was inserted into the solution through the rubber stopper for the whole measurement. The suspension was thoroughly degassed to remove air with CO_2 gas for 30 min with vigorous magnetic stirring. CO_2 gas (Airgas, Inc.) was bubbled through a deionized H_2O bubbler glassware to prepare the CO_2/H_2O gas mixture. The initial drop of O_2 was due to this purge of air out of the bottle. The suspension was illuminated using the Xe lamp at a power of 204 W with continuous CO_2/H_2O gas flow for the oxygen evolution measurements under illuminated conditions. Then the lamp was turned off for about 30 min for the oxygen evolution measurements under dark conditions. This light on/off cycle was repeated for several cycles.

Carbon isotope tracer measurements. The $^{13}CO_2$ (^{13}C 99%) was purchased from Cambridge Isotope Laboratories, Inc. Here 0.01 g of purified particles were dispersed in 5 ml of ultrapure deionized H_2O in a 20-ml Agilent Headspace vial and sealed. Then N_2 was used to purge the air from the vial for 2 min followed by three freeze–pump–thaw cycles to degas the photocatalyst suspension. After degassing, the $^{13}CO_2$ was introduced into the photocatalyst suspension by flushing isotope gas into the vial for 60 s. Then the samples were irradiated using a 300 W Xe lamp (Perkin-Elmer Optoelectronics) at a power of 204 W for 2 min at the same distance as for the photocatalytic activity measurements. The photocatalytic product was measured (Supplementary Fig. 8) using an Agilent Headspace sampler (model 7697 A) connected to an Agilent GC–MS analyser (model 5975C GC–MS, with quadrupole detector, TCD detector, DB-5ms column and helium carrier gas).

Oxygen isotope tracer measurements. The $H_2{}^{18}O$ (^{18}O, 97%) was purchased from Cambridge Isotope Laboratories, Inc and the $^{18}O_2$/helium mixture (ratio 1:9) from Sigma Aldrich. The $^{18}O_2$/helium mixture (ratio 1:9) or $^{16}O_2$ was injected for calibration of GC. Then 0.01 g of purified particles were dispersed in 5 ml of $H_2{}^{18}O$ in a 20-ml Agilent Headspace vial and sealed. Then N_2 was used to purge the air from the vial for 2 min followed by three freeze–pump–thaw cycles to degas the photocatalyst suspension. After degassing, the $^{13}C^{16}O_2$ was introduced into the photocatalyst suspension by flushing isotope gas into the vial for 60 s (^{13}C was used to change the molecular weight of methanol from 32 to 33 and differentiate it from $^{16}O_2$). Then the samples were illuminated using a 300 W Xe lamp (Perkin-Elmer Optoelectronics) at a power of 204 W for 2 min at the same distance as for the photocatalytic activity measurements. The oxygen from the photocatalytic reaction was measured (Supplementary Fig. 6) using an Agilent Headspace sampler (model 7697A) connected to an Agilent GC–MS analyser (model 5975C GC–MS, with quadrupole detector, TCD detector, DB-5ms column and helium carrier gas).

Quantum yield determination. Actinometry was used to determine the photon flux from the Xe lamp with the same power (204 W) and distance from the optical source to the sample as for the photocatalytic reaction. Since Cu_2O has a band gap of 2.1 eV (~590 nm), we chose iron(III) oxalate as the standard chemical actinometry following the International Union of Pure and Applied Chemistry (IUPAC)[56]. Iron(III) oxalate hexahydrate ($Fe_2(C_2O_4)_3{\bullet}6H_2O$), ammonium iron(II) sulfate hexahydrate ($(NH_4)_2[Fe(SO_4)_2]{\bullet}6H_2O$), 1,10-phenathroline, sodium acetate (CH_3COONa) and sulfuric acid were purchased from Sigma Aldrich.

Then 1,10-phenathroline was used for photometric determination of Fe^{2+} by forming $[Fe(phen)_3]^{2+}$, which has strong absorption at 510 nm. The molar absorptivity of $[Fe(phen)_3]^{2+}$ was determined by using ammonium iron(II) sulfate and 1,10-phenathroline. A 0.4 mM Fe^{2+} iron solution was made freshly by dissolving 0.00392 g of $(NH_4)_2[Fe(SO_4)_2]{\bullet}6H_2O$ with 25 ml of 0.05 M H_2SO_4 solution. Then 0, 0.75, 1.25, 1.75 and 3 ml of 0.4 mM Fe^{2+} solution were added to a series of 25 ml volumetric flasks and mixed with 1.25 ml of 0.5 M H_2SO_4, 6.25 ml of buffer solution (with stock solution of 3.82 g of $NaC_2H_5CO_2$, 0.4 ml of concentrated H_2SO_4, diluted to 40 ml with deionized water) and 5 ml of 0.1% 1,10-phenantroline solution (stored in the dark), before dilution to 25 ml with deionized water. The mixture was kept in the dark for about 60 min when full colour development was achieved. The mixture contained concentrations of $[Fe(phen)_3]^{2+}$ ions ranging from 0 to 4.8×10^{-5} M. The molar absorptivity ε of $[Fe(phen)_3]^{2+}$ was determined to be $0.89\times10^4\,l\,cm^{-1}\,mol^{-1}$ by measuring the concentration-dependent absorbance at 510 nm (Supplementary Fig. 4), which is close to the suggested value of $1.1\times10^4\,l\,cm^{-1}\,mol^{-1}$ (ref. [56]). This measured value was used for calculating the photon flux from the white light source.

A 0.006 M Fe^{3+} solution was prepared by dissolving 0.05806 g of $Fe(C_2O_4)_3{\bullet}6H_2O$ in 2 ml of H_2SO_4 (0.5 M) before dilution with deionized water to 20 ml. Then 3 ml (V_1) of the solution was illuminated for certain lengths of time, t, (5, 15, 25, 30, 35 s) under efficient magnetic stirring with the white light source power at 204 W (the same power for the photocatalytic activity measurement). A 1 ml volume (V_2) of the illuminated solution was added to a 10 ml (V_3) volumetric flask containing a mixture of 5 ml of 0.1% 1,10-phenantroline solution (stored in the dark) and 0.5 ml of buffer solution, which was then diluted to a total volume of 10 ml. A reference sample was prepared in the same way except it was not illuminated. The production of Fe^{2+} from Fe^{3+} can be summarized by the following photochemical reaction:

$$2\left[Fe(C_2O_4)_3\right]^{3-} + h\nu \rightarrow 2\left[Fe(C_2O_4)_2\right]^{2-} + 2CO_2 + C_2O_4^{2-} \qquad (1)$$

Where h is the Planck constant and ν is light frequency. All the solutions were stored in the dark for about 60 min until full colour development was achieved. The absorbance difference between the experimental samples and the reference sample was measured at 510 nm (optical path length $l=1$ cm, $\varepsilon(510\,\mathrm{nm})=0.89\times10^4\,\mathrm{l\,cm^{-1}\,mol^{-1}}$). A 0.2 ml volume ($V_4$) of solution was taken from 10 ml (V_3) of fully developed solution and then diluted to 3.2 ml (V_5) in an optical cuvette to ensure the absorbance A (510 nm) was within the range 0.3–1.1 (Supplementary Fig. 4). The number of moles, n, of Fe^{2+} produced by the photochemical reaction is given by

$$n=\frac{\Delta A V_1 V_3 V_5}{\varepsilon l V_2 V_4} \tag{2}$$

Where ΔA is the change of absorbance after illumination with time period, t. The photon flux q (einstein s^{-1}) entering the sample cell is

$$q=\frac{n}{t\Phi}=\frac{\Delta A V_1 V_3 V_5}{t\Phi\varepsilon l V_2 V_4} \tag{3}$$

The slope of $\frac{n}{t}$ was measured to be $9.28661\times10^{-4}\,\mathrm{mol\,s^{-1}}$ (Supplementary Fig. 4), and since the quantum yield of reaction (1), $\Phi_{Fe^{2+}}$ (510 nm) = 84.5% (ref. [57]), q is calculated to be 1.099×10^{-3} einstein s^{-1} for the white light source at 204 W.

The internal quantum yield (IQY) of methanol production is given by

$$\mathrm{IQY}=\frac{6\times\text{the number of produced methanol molecules}}{q t_{\mathrm{irradiation}}} \tag{4}$$

When $t_{\mathrm{irradiation}}=120$ s, with 16 mmol methanol produced (Fig. 1), the IQY is given by

$$\mathrm{IQY}=\frac{6\times16\times10^{-3}}{1.099\times10^{-3}\times120}=72.8\% \tag{5}$$

Ultraviolet–visible (UV–vis) absorption was measured using a Perkin-Elmer Lambda 950 UV–vis spectrometer (Supplementary Fig. 21). The wavelength dependences of the internal quantum yield[58](the number of electrons for methanol production per absorbed photons) and apparent quantum yield[58] (the number of electrons for methanol production per incident photons) were measured using 0. 01 g of Cu_2O purified particles in 5 ml of ultrapure deionized H_2O with continuous CO_2/H_2O gas flow. An Xe lamp with the same power (204 W) and distance from the optical source to the sample were used for the photocatalytic reactions with 2 min irradiation time. Illumination was carried out with a 20-cm-long quartz infrared water filter. This cuts off the photons of the infrared region to minimize heating on the sample. Various bandpass filters were applied to select portions of the incident photons. The entire visible light solar spectrum was divided into ten intervals: 400–435 nm, 435–475 nm, 475–500 nm, 500–530 nm, 530–550 nm, 550–570 nm, 570–600 nm, 600–640 nm, 640–680 nm and 680–700 nm. The amount of methanol at certain wavelengths was determined by GC. Wavelength-dependent internal quantum yield and apparent quantum yield are shown in Supplementary Fig. 22. The wavelength-dependent apparent quantum yield correlates well with the wavelength dependence of the photon absorption by Cu_2O (UV–vis absorption spectrum in Supplementary Fig. 20). On the other hand, the wavelength dependence of the internal quantum yield tells us some useful information about the nature of the photoexcitation process. We find that there are very few losses for the initial condition of reduction of CO_2 to methanol with near band-gap excitation (~94% at 620 nm). However, we observe some losses in the high-energy excitation, consistent with the thermalization of photogenerated charges to the band edges. This, in turn, lowers the internal quantum yield to ~50% at 400 nm. The overall internal quantum yield in the visible light region is around 72%. The overall external quantum yield in the visible light region is about 23%. This proves that the reaction is driven by light.

Solar-to-fuel efficiency calculation from apparent quantum yield data. The solar-to-fuel efficiency (STF) in the visible light region was calculated from the apparent quantum yield data from Supplementary Fig. 22. This solar energy conversion was evaluated using the same white light source as for the quantum yield measurement with Cu_2O photocatalyst (0.01 g of photocatalyst in 5 ml of de-ionized water). Illumination was carried out with a 20-cm-long quartz infrared water filter. This cuts off the photons of the infrared region to minimize heating on the sample. Methanol and oxygen were measured as reaction products in the Agilent Headspace sampler as the reactor. The reactor is made of 33–51 coefficient of expansion type I borosilicate glass. A possible chemical formula describing the reaction is the following:

$$\mathrm{CO_2+2H_2O\rightarrow CH_3OH+\frac{3}{2}O_2} \tag{6}$$

The Gibbs free energy (ΔG) of this formula to produce CH_3OH was suggested to be 638.73 kJ mol^{-1} (or 6.62 eV per molecule)[39].

$$\mathrm{STF}=\frac{\text{Energy of generated }\mathrm{CH_3OH}}{\text{Solar energy irradiating the solution}}=\frac{E_{\mathrm{CH_3OH}}}{E_{\mathrm{solar}}} \tag{7}$$

$$E_{\mathrm{CH_3OH}}=\sum_i \text{number of generated }\mathrm{CH_3OH}\times\Delta\mathrm{G} \tag{8}$$

$$\begin{aligned}\sum_i \mathrm{AQY}(\lambda_i)&=\sum_i\frac{\text{number of generated electrons}}{n_{\mathrm{photon,i}}}\\&=\sum_i\frac{6\times\text{number of generated }\mathrm{CH_3OH}}{n_{\mathrm{photon,i}}}\end{aligned} \tag{9}$$

Here, $n_{\mathrm{phonon},\,i}$ is the number of photons with wavelength λ in interval i and $\mathrm{AQY}(\lambda_i)$ is the apparent quantum yield of the ith interval in the range.

$$E_{\mathrm{CH_3OH}}=\sum_i n_{\mathrm{photon,i}}\times\mathrm{AQY}(\lambda_{\mathrm{i}})\times\frac{1}{6}\times6.62\,\mathrm{eV}\times1.602\times10^{-19}\,\mathrm{J\,eV^{-1}} \tag{10}$$

Thus, we get

$$\mathrm{STF}=\sum_i\frac{n_{\mathrm{photon,i}}\times\mathrm{AQY}(\lambda_{\mathrm{i}})\times6.62\,\mathrm{eV}\times1.602\times10^{-19}\,\mathrm{J\,eV^{-1}}\times\frac{1}{6}}{E_{\mathrm{solar}}} \tag{11}$$

In order to derive number of photons per interval i, $n_{\mathrm{photon},i}$, solar energy irradiating the solution should be divided into intervals $E_{\lambda i}$, with p_i being the fraction of solar power in interval i:

$$\sum_i p_i\times E_{\mathrm{solar}}=\sum_i E_{\lambda_i} \tag{12}$$

$$\sum_i E_{\lambda_i}=\sum_i n_{\mathrm{phonon,i}}\times\frac{hc}{\lambda_i} \tag{13}$$

Combining equations (12) and (13), we get

$$n_{\mathrm{phonon,i}}=\frac{p_i\times E_{\mathrm{solar}}\times\lambda_i}{hc}=\frac{p_i\times E_{\mathrm{solar}}\times\lambda_i}{6.626\times10^{-34}\times3\times10^8} \tag{14}$$

Where c is the speed of light. Combining equations (11) and (14), we get

$$\mathrm{STF}=\sum_i\frac{p_i\times\lambda_i\times6.62\times1.602\times10^{-19}\times\frac{1}{6}}{19.86\times10^{-26}}\times\mathrm{AQY}(\lambda_{\mathrm{i}}) \tag{15}$$

$$\mathrm{STF}=\sum_i 0.89\times10^6\times p_i\times\lambda_i\times\mathrm{AQY}(\lambda_{\mathrm{i}}) \tag{16}$$

Since the photons of the infrared region were cut off by a 20-cm-long quartz infrared water filter, the visible region of the solar spectrum was divided into ten intervals ($i=1, 2, 3, \ldots,10$). The fraction of solar power in interval i was calculated by dividing the area of interval i of the spectrum by the entire area of the solar spectrum distribution of the light source. The calculated solar-to-fuel efficiency is about 10.1% as shownsc in Supplementary Table 1. This is less than the theoretical prediction maximum of 35.2% for methanol[39].

Operando multimodal single-particle microscopy and nanospectroscopy. We used a custom gas-flow nanoreactor (Hummingbird Scientific) to examine single Cu_2O particles under working conditions by in situ ETEM and operando SFXM. The Cu_2O particles were sandwiched inside the nanoreactor between 50 nm Si_3N_4 membranes through which CO_2 and H_2O gas were flowed at atmospheric pressure (Fig. 2a). The optical transparency of the Si_3N_4 membranes facilitated excitation of the photocatalyst with a laser whilst probing the structure and chemical state of the Cu_2O particles (Fig. 2a and Supplementary Fig. 9). This enabled us to study the same photocatalytic particle under working conditions by both in situ ETEM and operando SFXM (Supplementary Figs 6, 12). Nickel grid bars on the bottom membrane served as fiducial marks to identify the same particle in the nanoreactor with both techniques (Fig. 2c).

Cu_2O particles were dispersed in ethanol and drop-casted onto the bottom Si chip with a Si_3N_4 membrane and nickel grid bars. The bottom Si chip was assembled with a top Si chip, which also had a Si_3N_4 membrane, and separated by spacers. Samples were maintained in the nanoreactor under stable environmental conditions during transfer between the ETEM and SFXM platforms. For the in situ ETEM and operando SFXM measurements, CO_2 gas (Airgas, Inc.) and H_2O vapour gas (500 ppm mol percentage balance with N_2 (Airgas, Inc.), 500 mol H_2O molecules per 1 million moles of N_2 molecules) were mixed and delivered to the nanoreactor at 0.05 sccm using a gas-flow control box (Hummingbird Scientific). The CO_2 to H_2O (gas) pressure ratio was about 1:1. ETEM imaging and EELS were performed on a JEOL 2100F electron microscope operated at an accelerating voltage of 200 kV and equipped with a Gatan imaging filter system with an energy dispersion of 0.05 eV per pixel at the Center for Nanoscale Materials (CNM) at Argonne National Laboratory. EELS spectra were recorded in energy-filter TEM mode with an energy resolution of 0.7 eV, a collimated beam and 1 nm probe size. Exposure of the sample to the electron beam was minimized to avoid damage. Gas flow was started with closed beam valve for 30 min before taking EELS spectra with the gas mixture. An EELS acquisition time of 5 s and zero-loss peak calibration were performed between each acquisition to prevent zero-loss peak drift from microscope instabilities by the introduction of the gas. The threshold dose rate for electron beam damage on metal oxide was suggested to be 3.125×10^3 $e^- s^{-1} Å^{-2}$ (or $5 A cm^{-2}$)[59], while the dose rate used in this experiment was about $1.5 \times 10^2 e^- s^{-1} Å^{-2}$. This is about an order of magnitude smaller than the threshold of beam damage for metal oxide. This published threshold is in agreement with our experimental observation that no obvious structural damage occurred. SFXM was performed using the Hard X-ray Nanoprobe[60] operated by the CNM at beamline 26-ID at the Advanced Photon Source (APS) at Argonne National Laboratory. A Fresnel zone plate lens with a 20 nm finest zone focused a coherent, monochromatic ~9 keV X-ray beam to a ~30 nm spot with an intensity of 10^9 photons s^{-1}. A four-element silicon drift detector (Vortex ME4) collected the emitted characteristic fluorescence X-rays. The sample was illuminated with either a green (532 nm) or blue (445 nm) laser to induce photocatalysis. The X-ray microscopy experiment setup is shown in Supplementary Fig. 9. TEM measurements made on the same particle afterwards show the particle was stable during the X-ray measurements (Supplementary Fig. 11). Reference X-ray absorption spectroscopy data were taken with Cu, Cu_2O and CuO powder standards at APS beamline 20-ID-B for comparison (Supplementary Fig. 11).

Operando high-energy X-ray diffraction characterization. We performed operando high-energy X-ray diffraction characterization during the CO_2 adsorption under dark and illuminated conditions at APS beamline 11-ID-C. A Si(311) single-crystal monochromator, with X-ray beam energy of 105.1 keV, beam size of $0.2 \times 0.2 mm^2$ and a Perkin-Elmer area detector located at 1.8 m were used to obtain 2D diffraction patterns from the sample. The Cu_2O ensemble was placed in a glass pipette partially sealed with glass fibres, which was connected to the same gas-delivering system used for in situ single-particle ETEM and operando SFXM. Then the photocatalyst was irradiated using the Xe lamp with continuous CO_2/H_2O gas flow during the measurement. Diffraction data from the sample were recorded every 30 s. The obtained 2D diffraction patterns were calibrated using a standard CeO_2 sample, converted to one-dimensional patterns using the Fit2D software package[61], then analysed using the ranked data analysis software package[62].

Ex situ high-resolution synchrotron X-ray powder diffraction. Synchrotron HRXRD data were collected at APS beamline 11-BM-B, using a wavelength of 0.414230 Å for the CO_2/H_2O treated samples (Fig. 5 and Supplementary Fig. 17) and a wavelength of 0.414221 Å for the H_2O treated samples (Supplementary Fig. 18). All samples were sealed by Varian Torr Seal epoxy in Kapton capillaries inside a N_2 gas-flow glove box. All diffraction patterns were collected at room temperature. Discrete patterns covering an angular range of 4–12° were scanned over a 25° range in 2θ, with data points collected every 0.001° using a scan speed of 0.1 s per step.

Ex situ structural characterization. SEM images of the photocatalyst particles were taken with a JEOL 7500 scanning electron microscope with an acceleration voltage of 10 kV. Transmission electron microscope and high-resolution TEM images (Supplementary Fig. 23), NBD and EELS measurements were performed with a JEOL 2100F electron microscope operated at an accelerating voltage of 200 kV and equipped with a Gatan imaging filter system at the CNM. Ex situ TEM characterization was performed by drop casting a suspension of the photocatalyst particles in ethanol onto a Formvar-coated Au TEM grid.

EPR characterization. Continuous-wave EPR measurements were carried out using a Bruker ELEXYS E580 spectrometer operating in the X-band (9.4 GHz) mode and equipped with an Oxford CF935 helium flow cryostat with an ITC-5025 temperature controller at CNM. The g tensor was calibrated for homogeneity and accuracy by comparison to a standard 1,3 Bisdiphenilene 2 phenylallyl benzene (BDPA-benzene) complex, with $g = 2.00254 \pm 0.00005$. The receiver gain and number of scans were adjusted for each spectrum of a particular sample to enable comparison at the same signal-to-noise ratio. The measurements were carried out at 4 K. For the studies of charge transfer, samples were degassed by bubbling in a N_2 flow glove box, frozen at liquid He temperature and illuminated in the EPR cavity using the 300 W Xe lamp with a plano-convex lens (50 cm focal length) with a broadband antireflection coating and water as an infrared cutoff filter.

We used 0.01 g of Cu_2O in the EPR experiment. The number of Cu_2O molecules is n_a:

$$n_a = \frac{m}{M} N_A = \frac{0.01\,\text{g}}{143\,\text{g mol}^{-1}} \times 6.02 \times 10^{23} = 4.2 \times 10^{19} \tag{17}$$

Where N_A is Avogadro's number. The number of spins from the Cu cluster was determined to be 3×10^{12} (~4.98×10^{-12} mol) by comparing the signal to the calibrated weak pitch sample under the same conditions. Assuming that the Cu clusters are produced from the Cu(I) disproportionation reaction under illumination according to the reaction:

$$Cu_2O = Cu^0 + Cu^{2+} + \frac{1}{2}O_2 \tag{18}$$

The number of O_2 molecules produced by disproportionation, $n_b = 1.5 \times 10^{12}$ O_2 molecules.

With the same amount of illumination, we measured 22 μmol of O_2. The number of O_2 molecules is n_c:

$$n_c = nN_A = 2.2 \times 10^{-5} \times 6.02 \times 10^{23} = 1.32 \times 10^{19} \tag{19}$$

Since n_b is seven orders of magnitude less than n_c, O_2 measured under illumination does not only originate from Cu(I) disproportionation.

DFT calculations. To study the stability of both the pristine surfaces and adsorption of CO_2 and H_2O on surfaces of the Cu_2O particles, we performed DFT calculations with plane-wave basis sets as implemented in the VASP code[63,64]. All the calculations were spin-polarized and carried out using the gradient corrected exchange-correlation functional of Perdew, Burke and Ernzerhof[65] under the projector augmented wave method, with plane-wave basis set up for a kinetic energy cutoff of 500 eV. The projector augmented wave method[66] was used to represent the interaction between the core and valence electrons, and the Kohn–Sham valence states (that is 1*s* for H, 2*s*2*p* for C and O, 3*d*4*s* for Cu) are expanded in plane-wave basis sets. For both the Cu_2O bulk crystal and surface calculations, the GGA + U calculations were followed, with the Hubbard U value of Cu atoms chosen to be $U = 6.0$ eV, according to the reported Cu_2O compounds in the literature[67]. For the geometry optimization, the convergence criterion of the total energy was set to be within 1×10^{-5} eV for the K-point integration, and all the atoms and geometries were optimized until the residual forces became less than 1×10^{-2} eV $Å^{-1}$. For the Cu_2O bulk crystal, the calculation was based on a mesh of $8 \times 8 \times 8$ in the K-point grid. For both the crystalline Cu_2O surfaces (that is, (110) and (100) surfaces) and adsorption calculations, a K-point grid of $2 \times 2 \times 1$ was used. For the surface slab calculations, we adopted a slab/vacuum geometry composed of repeating slabs and vacuum layers. In the supercell of the surface slab calculations, the vacuum thickness was ~18 Å and the thickness of the surface slab was ~22 Å, over which the bottom three layers were fixed in the crystalline bulk position during the geometry optimization. Calculated conformations of linear and bent CO_2 (that is, activated CO_2)[68] on Cu termination of Cu_2O (110) with the co-adsorption of H_2O are shown in Supplementary Fig. 14.

Photoreduction of metal salts on Cu_2O. The photoreduction of metal ions on the surface of particles was carried out using $HAuCl_4$ as precursor and H_2O as hole scavenger. Specifically, 5 mg of Cu_2O particles were mixed with 10 mg of $HAuCl_4$ in 10 ml of de-ionized H_2O. The suspension was irradiated with a 300 W Xe lamp for 2 min with continuous stirring. Then the suspension was filtered and washed with de-ionized H_2O and dried in a glove box for 48 h. The Au nanoparticles were deposited randomly on Cu_2O without preferable facets (Supplementary Fig. 20).

Data availability

The data that support the plots within this paper and the findings of this study are available from the corresponding authors upon reasonable request.

Received: 30 August 2018; Accepted: 27 September 2019;
Published online: 04 November 2019

References

1. Liu, C. et al. Carbon dioxide conversion to methanol over size-selected Cu_4 clusters at low pressures. *J. Am. Chem. Soc.* **137**, 8676–8679 (2015).
2. Yu, K. M. K., Yeung, C. M. Y. & Tsang, S. C. Carbon dioxide fixation into methyl formate by surface couple over a Pd/Cu/ZnO nanocatalyst. *J. Am. Chem. Soc.* **129**, 6360–6361 (2007).
3. Liao, F. Morphology-dependent interactions of ZnO with Cu nanoparticles at the materials' interface in selective hydrogenation of CO2 to CH3OH. *Angew. Chemie Int. Ed.* **50**, 2162–2165 (2011).
4. Graciani, J. et al. Highly active copper-ceria and copper-ceria-titania catalysts for methanol synthesis from CO_2. *Science* **345**, 546–550 (2014).
5. Tang, W. et al. The importance of surface morphology in controlling the selectivity of polycrystalline copper for CO_2 electroreduction. *Phys. Chem. Chem. Phys.* **14**, 76–81 (2012).
6. Chen, Y., Li, C. W. & Kanan, M. W. Aqueous CO_2 reduction at very low overpotential on oxide-derived Au nanoparticles. *J. Am. Chem. Soc.* **134**, 19969–19972 (2012).
7. Li, C. W. & Kanan, M. W. CO_2 reduction at low overpotential on Cu electrodes resulting from the reduction of thick Cu_2O films. *J. Am. Chem. Soc.* **134**, 7231–7234 (2012).
8. Li, C. W., Ciston, J. & Kanan, M. W. Electroreduction of carbon monoxide to liquid fuel on oxide-derived nanocrystalline copper. *Nature* **508**, 504–507 (2014).
9. Asadi, M. et al. Nanostructured transition metal dichalcogenide electrocatalysts for CO_2 reduction in ionic liquid. *Science* **353**, 467–470 (2016).

10. Liu, C., Colon, B. C., Ziesack, M., Silver, P. A. & Nocera, D. G. Water splitting-biosynthetic system with CO_2 reduction efficiencies exceeding photosynthesis. *Science* **352**, 1210–1213 (2016).
11. Gao, S. et al. Partially oxidized atomic cobalt layers for carbon dioxide electroreduction to liquid fuel. *Nature* **529**, 68–71 (2016).
12. Melchionna, M. et al. Pd@TiO_2/carbon nanohorn electrocatalysts: reversible CO_2 hydrogenation to formic acid. *Energy Environ. Sci.* **11**, 1571–1580 (2018).
13. Styring, S. Artificial photosynthesis for solar fuels. *Faraday Discuss.* **155**, 357–376 (2012).
14. Liu, J. et al. Metal-free efficient photocatalyst for stable visible water splitting via a two-electron pathway. *Science* **347**, 970–974 (2015).
15. Halmann, M. Photoelectrochemical reduction of aqueous carbon dioxide on p-type gallium phosphide in liquid junction solar cells. *Nature* **275**, 115–116 (1978).
16. Tamaki, Y., Morimoto, T., Koike, K. & Ishitani, O. Photocatalytic CO_2 reduction with high turnover frequency and selectivity of formic acid formation using Ru(II) multinuclear complexes. *Proc. Natl Acad. Sci. USA* **109**, 15673–15678 (2012).
17. Sekizawa, Keita, Maeda, Kazuhiko, Domen, Kazunari, Koike, K. & Ishitani, O. Artificial Z scheme constructed with a supramolecular metal complex and semiconductor for the photocatalytic reduction of CO_2. *J. Am. Chem. Soc.* **135**, 4596–4599 (2013).
18. Qiu, J. et al. Artificial photosynthesis on TiO_2 -passivated InP nanopillars. *Nano Lett.* **15**, 6177–6181 (2015).
19. Kothandaraman, J., Goeppert, A., Czaun, M., Olah, Ga & Prakash, G. K. S. Conversion of CO_2 from air into methanol using a polyamine and a homogeneous ruthenium catalyst. *J. Am. Chem. Soc.* **138**, 778–781 (2016).
20. Liu, C. et al. Nanowire-bacteria hybrids for unassisted solar carbon dioxide fixation to value-added chemicals. *Nano Lett.* **15**, 3634–3639 (2015).
21. Paria, S. & Reiser, O. Copper in photocatalysis. *ChemCatChem* **6**, 2477–2483 (2014).
22. Kainz, Q. M. et al. Asymmetric copper-catalyzed C-N cross-couplings induced by visible light. *Science* **351**, 681–684 (2016).
23. Angamuthu, R., Byers, P., Lutz, M., Spek, A. L. & Bouwman, E. Electrocatalytic CO_2 conversion to oxalate by a copper complex. *Science* **327**, 313–315 (2010).
24. Reske, R., Mistry, H., Behafarid, F., Cuenya, B. R. & Strasser, P. Particle size effects in the catalytic electroreduction of CO_2 on Cu nanoparticles. *J. Am. Chem. Soc.* **136**, 6978–6986 (2014).
25. Roberts, F. S., Kuhl, K. P. & Nilsson, A. High selectivity for ethylene from carbon dioxide reduction over copper nanocube electrocatalysts Angew. *Chemie Int. Ed.* **54**, 5179–5182 (2015).
26. Loiudice, A. et al. Tailoring copper nanocrystals towards C_2 products in electrochemical CO_2 reduction. *Angew. Chem. Int. Ed.* **55**, 5789–5792 (2016).
27. Mistry, H. et al. Highly selective plasma-activated copper catalysts for carbon dioxide reduction to ethylene. *Nat. Commun.* **7**, 12123 (2016).
28. Paracchino, A., Laporte, V., Sivula, K., Grätzel, M. & Thimsen, E. Highly active oxide photocathode for photoelectrochemical water reduction. *Nat. Mater.* **10**, 456–461 (2011).
29. Kwon, Y., Soon, A., Han, H. & Lee, H. Shape effects of cuprous oxide particles on stability in water and photocatalytic water splitting. *J. Mater. Chem. A* **3**, 156–162 (2015).
30. Cui, J. & Gibson, U. J. A simple two-step electrodeposition of Cu_2O/ZnO nanopillar solar cells. *J. Phys. Chem. C* **114**, 6408–6412 (2010).
31. Morales, J. et al. Electrodeposition of Cu_2O: an excellent method for obtaining films of controlled morphology and good performance in Li-ion batteries. *Electrochem. Solid-State Lett.* **8**, A159–A162 (2005).
32. Tran, P. D., Wong, L. H., Barber, J. & Loo, J. S. C. Recent advances in hybrid photocatalysts for solar fuel production. *Energy Environ. Sci.* **5**, 5902–5918 (2012).
33. Handoko, A. D. & Tang, J. Controllable proton and CO_2 photoreduction over Cu_2O with various morphologies. *Int. J. Hydrog. Energy* **38**, 13017–13022 (2013).
34. An, X., Li, K. & Tang, J. Cu_2O/reduced graphene oxide composites for the photocatalytic conversion of CO_2. *ChemSusChem* **7**, 1086–1093 (2014).
35. Christoforidis, K. C. & Fornasiero, P. Photocatalysis for hydrogen production and CO_2 reduction: the case of copper-catalysts. *ChemCatChem* **11**, 368–382 (2019).
36. Stolarczyk, J. K., Bhattacharyya, S., Polavarapu, L. & Feldmann, J. Challenges and prospects in solar water splitting and CO_2 reduction with inorganic and hybrid nanostructures. *ACS Catal.* **8**, 3602–3635 (2018).
37. Zheng, X. et al. Theory-driven design of high-valence metal sites for water oxidation confirmed using in situ soft X-ray absorption. *Nat. Chem.* **10**, 149–154 (2018).
38. Song, Y. et al. High-selectivity electrochemical conversion of CO_2 to ethanol using a copper nanoparticle/n-doped graphene electrode. *ChemistrySelect* **1**, 6055–6061 (2016).
39. Singh, M. R., Clark, E. L. & Bell, A. T. Thermodynamic and achievable efficiencies for solar-driven electrochemical reduction of carbon dioxide to transportation fuels. *Proc. Natl Acad. Sci. USA* **112**, E6111–E6118 (2015).
40. Chueh, W. C., Abbott, M., Scipio, D. & Haile, S. M. High-flux solar-driven thermochemical dissociation of CO_2 and H_2O using nonstoichiometric ceria. *Science* **330**, 1797–1801 (2010).
41. Koroidov, S., Anderlund, M. F., Styring, S., Thapper, A. & Messinger, J. First turnover analysis of water-oxidation catalyzed by Co-oxide nanoparticles. *Energy Environ. Sci.* **8**, 2492–2503 (2015).
42. Grimaud, A. et al. Activating lattice oxygen redox reactions in metal oxides to catalyse oxygen evolution. *Nat. Chem.* **9**, 457–465 (2017).
43. Rajh, T., Ostafin, A. E., Micic, O. I., Tiede, D. M. & Thurnauer, M. C. Surface modification of small particle TiO_2 colloids with cysteine for enhanced photochemical reduction: an EPR study. *J. Phys. Chem.* **100**, 4538–4545 (1996).
44. Wu, Y. A. et al. Visualizing redox dynamics of a single Ag/AgCl heterogeneous nanocatalyst at atomic resolution. *ACS Nano* **10**, 3738–3746 (2016).
45. Li, Y. et al. Complex structural dynamics of nanocatalysts revealed in operando conditions by correlated imaging and spectroscopy probes. *Nat. Commun.* **6**, 7583 (2015).
46. Wang, Z. L. New developments in transmission electron microscopy for nanotechnology. *Adv. Mater.* **15**, 1497–1514 (2003).
47. Yoshida, H. et al. Visualizing gas molecules interacting with supported nanoparticulate catalysts at reaction conditions. *Science* **335**, 317–319 (2012).
48. Watari, M. et al. Differential stress induced by thiol adsorption on facetted nanocrystals. *Nat. Mater.* **10**, 862–866 (2011).
49. Symons, M. C. R. *Chemical and Biochemical Aspects of Electron-spin Resonance Spectroscopy* (Wiley, 1978).
50. Hulliger, J., Zoller, L. & Ammeter, J. H. Orientation effects in EPR powder samples induced by the static magnetic field. *J. Magn. Reson.* **48**, 512–518 (1982).
51. Symons, M. C. R., West, D. X. & Wilkinson, J. G. Co-ordination of copper(II) ions doped in pentacyanonitrosylferrate(2-) and tetrathiocyanatometallate(II) salts: an electron spin resonance study. *J. Chem. Soc., Dalton Trans.* **16**, 1696–1700 (1975).
52. Grechnev, G. E., Savchenko, N. V., Svechkarev, I. V., Lee, M. J. G. & Perz, J. M. Conduction-electron g factors in the noble metals. *Phys. Rev. B* **39**, 9865–9873 (1989).
53. Liu, C., He, H., Zapol, P. & Curtiss, L. A. Computational studies of electrochemical CO_2 reduction on subnanometer transition metal clusters. *Phys. Chem. Chem. Phys.* **16**, 26584–26599 (2014).
54. Li, R. et al. Spatial separation of photogenerated electrons and holes among {010} and {110} crystal facets of $BiVO_4$. *Nat. Commun.* **4**, 1432 (2013).
55. Wang, X. et al. Controlled synthesis of concave Cu_2O microcrystals enclosed by {hhl} high-index facets and enhanced catalytic activity. *J. Mater. Chem. A* **1**, 282–287 (2013).
56. Kuhn, H. J., Braslavsky, S. E. & Schmidt, R. Chemical actinometry (IUPAC Technical Report). *Pure Appl. Chem.* **76**, 2105–2146 (2004).
57. Demas, J. N., Bowman, W. D., Zalewski, E. F. & Velapoldi, R. A. Determination of the quantum yield of the ferrioxalate actinometer with electrically calibrated radiometers. *J. Phys. Chem.* **85**, 2766–2771 (1981).
58. Braslavsky, S. E. et al. Glossary of terms used in photocatalysis and radiation catalysis (IUPAC Recommendations 2011). *Pure Appl. Chem.* **83**, 931–1014 (2011).
59. Jiang, N. Electron beam damage in oxides: a review. *Rep. Prog. Phys.* **79**, 016501 (2016).
60. Winarski, R. P. et al. A hard X-ray nanoprobe beamline for nanoscale microscopy. *J. Synchrotron Rad.* **19**, 1056–1060 (2012).
61. Hammersley, A. P., Svensson, S. O., Hanfland, M., Fitch, A. N. & Hausermann, D. Two-dimensional detector software: from real detector to idealised image or two-theta scan. *High. Press. Res.* **14**, 235–248 (1996).
62. Aoun, B. et al. A generalized method for high throughput *in-situ* experiment data analysis: an example of battery materials exploration. *J. Power Sources* **279**, 246–251 (2015).
63. Kresse, G. & Joubert, D. From ultrasoft pseudopotentials to the projector augmented-wave method. *Phys. Rev. B* **59**, 1758–1775 (1999).
64. Kresse, G. & Furthmüller, J. Efficiency of *ab-initio* total energy calculations for metals and semiconductors using a plane-wave basis set. *Comput. Mater. Sci.* **6**, 15–50 (1996).
65. Perdew, J. P., Burke, K. & Ernzerhof, M. Generalized gradient approximation made simple. *Phys. Rev. Lett.* **77**, 3865–3868 (1996).
66. Blöchl, P. E. Projector augmented-wave method. *Phys. Rev. B* **50**, 17953–17979 (1994).
67. Bendavid, L. I. & Carter, E. A. First-principles predictions of the structure, stability, and photocatalytic potential of Cu_2O surfaces. *J. Phys. Chem. B* **117**, 15750–15760 (2013).
68. Mishra, A. K., Roldan, A. & De Leeuw, N. H. A density functional theory study of the adsorption behaviour of CO_2 on Cu_2O surfaces. *J. Chem. Phys.* **145**, 044709 (2016).

Acknowledgements

This work was performed at the Center for Nanoscale Materials, a US Department of Energy, Office of Science, Basic Energy Sciences, under Contract no. DE-AC02-06CH11357. Use of the Advanced Photon Source was supported by the US Department of Energy, Office of Science, Office of Basic Energy Sciences, under Contract no. DE-AC02-06CH11357. This work is partially supported by Laboratory Directed Research and Development (LDRD) funding from Argonne National Laboratory, provided by the Director, Office of Science, of the US Department of Energy under Contract no. DE-AC02-06CH11357. The computational studies were supported by the US Department of Energy, Basic Energy Sciences, Division of Materials Science and Engineering. C.L., K.C.L. and L.A.C. acknowledge grants of computer time through the LCRC Blues Cluster at Argonne National Laboratory. Cong Liu acknowledges the financial support by US Department of Energy, Office of Basic Energy Sciences, Division of Chemical Sciences, Geosciences and Biosciences, under Contract no. DE-AC02-06CH11357. We acknowledge discussions with and the assistance of P. Fuesz, M. Holt, S. Lapidus, E. Rozhkova, C. Fry, R. Zhang, L. Li and M. Chan.

Author contributions

Y.A.W., I.M., Y.L. and T.R., conceived the ideas. Y.A.W. performed synthesis of samples, ex situ structural characterization, photocatalytic activity characterization, solar-to-fuel efficiency measurements and quantum yield measurements. Y.A.W., Z.C., J.R.G., Y.L. and I.M. performed operando SFXM measurements. Y.A.W. and Y.L. performed operando ETEM, electron diffraction and EELS measurements. Y.A.W. and T.R. performed EPR and isotope tracer measurements. Y.A.W., Q.L. and Y.R. performed operando high-energy X-ray diffraction and ex situ high-resolution X-ray powder diffraction measurements. Y.A.W. and C.-J.S. performed X-ray absorption spectroscopy measurements. A.P.P. and V.S. performed XPS measurements. C.L., K.C.L. and L.A.C. performed DFT computations. Y.A.W., I.M. and T.R. wrote the paper. All authors contributed to the discussion and revision of the paper.

Competing interests

The authors declare no competing interests.

Additional information

Supplementary information is available for this paper at https://doi.org/10.1038/s41560-019-0490-3.

Correspondence and requests for materials should be addressed to Y.L. or T.R.

Reprints and permissions information is available at www.nature.com/reprints.

Publisher's note Springer Nature remains neutral with regard to jurisdictional claims in published maps and institutional affiliations.

This is a U.S. government work and not under copyright protection in the U.S.; foreign copyright protection may apply 2019